1

The Fundamentals of Solar Energy Photocatalysis

Xin Li[1] *and Jiaguo Yu*[2]

[1] *Institute of Biomass Engineering, South China Agricultural University, 483 Wushan Road, Tianhe District, Guangzhou 510642, P. R. China*
[2] *China University of Geosciences, Laboratory of Solar Fuel, Faculty of Materials Science and Chemistry, 388 Lumo Road, Wuhan 430074, P. R. China*

1.1 Background

Solar energy semiconductor photocatalysis has long been considered to be the best solution to various kinds of energy and environmental problems. During the past decades, the solar energy semiconductor photocatalysis has attracted more and more attention. Based on Figure 1.1a, the total number of academic papers on the photocatalysis published since 1996 has reached 64 011, with increasing publication year by year. Especially, there are almost 8000 papers published in 2019 in the field of photocatalysis. Among all different research fields, the number of papers in photocatalytic pollutant degradation is the largest, which is much more than the total number of publications in both photocatalytic H_2 evolution and CO_2 reduction (Figure 1.1b).

So far, hundreds of solar energy semiconductor photocatalysts have been exploited and applied in the different photocatalytic fields, including the plasmonic metals, metal oxides/hydroxides, sulfides, nitrides, metal-free polymers, organic semiconductors, and their composites. Although some reviews covered the progresses of these kinds of semiconductors, there are few books systematically summarizing the advances in these semiconductors. Therefore, it is timely to provide a comprehensive book to thoroughly elaborate the exploitation and application of typical kinds of solar energy semiconductors in the different photocatalytic fields. We believe that this book can help the researchers easily grasp the recent achievements for various kinds of semiconductors and inspire their new ideas in developing new solar energy semiconductors for efficient photocatalysis.

1.2 History of Solar Energy Photocatalysis

Due to its green and renewable advantages, photocatalysis has been one of the most active directions in the field of chemistry in recent years.

Semiconductor Solar Photocatalysts: Fundamentals and Applications, First Edition.
Edited by Jiaguo Yu, Xin Li, and Jingxiang Low.

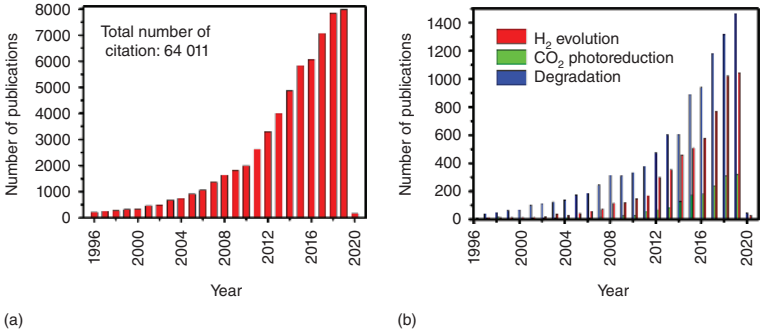

Figure 1.1 The number of publications on photocatalysis found by searching with the following keywords: (a) topic: (photoca*), (b) topic 1: (photoca*), and topic 2: (hydrogen or H-2 or H_2), (carbon dioxide or CO_2 or CO-2), or (degradat*). Source: Science Core Collection 26 November 2019.

Semiconductor photocatalysis can be traced back to 1839. Becquerel [1] first discovered the photoelectric phenomenon, although he did not explain it theoretically.

In 1955, Brattain and Garrett [2] gave a reasonable explanation for the photoelectric phenomena, marking the birth of photoelectrochemistry.

Especially in 1972, Fujishima and Honda first found that n-type semiconductor rutile TiO_2 single crystal electrode could achieve the photocatalytic decomposition of H_2O to O_2 under the ultraviolet (UV) light (with 380 nm wavelength), while on the counter electrode Pt simultaneously produces H_2 [3]. This great discovery has caused a sensation all over the world, which revealed the possibility of using solar energy to decompose water for hydrogen production – or to convert solar energy directly into chemical energy – thus opening up a new era of semiconductor photocatalysis research and attracting worldwide attention. Because of its far-reaching significance in the development of new energy and the protection of ecological environment, heterogeneous semiconductor photocatalysis has become a hot spot, attracting the extensive attention of researchers in many fields, such as chemistry, physics, and materials.

In the middle and late 1970s, Carey et al. [4] and Bard and coworker [5] utilized the TiO_2 suspension to degrade polychlorinated biphenyls and cyanides, respectively, under UV irradiation, which set off a research upsurge of environmental photocatalysis technology with the main purpose of decomposing environmental pollutants.

Schrauzer also confirmed that TiO_2 with rutile and anatase mixed crystal phases can realize the photocatalytic decomposition of chemisorbed water into H_2 and O_2 with a 2 : 1 stoichiometric ratio [6].

At the same time, Bard and his coworkers have guided and promoted the development of photoelectrochemistry. They first extended the theory of photoelectrochemistry (microelectrode model) to the photocatalysis of semiconductor particles, advancing the semiconductor photocatalysis technology greatly in theory. They not only used electron paramagnetic resonance (EPR) spectroscopy to characterize the free radicals such as hydroxyl (·OH) and hydroperoxyl (·OOH) radicals in the processes of photocatalytic oxidation and photocatalytic reduction of O_2 [7, 8],

respectively, but also used Pt-decorated TiO_2 photocatalyst to decompose acetic acid for generating methane (CH_4), which proved that the heterogeneous photocatalysis process has similar principles to the photoelectrochemical (PEC) process [9, 10]. In terms of its charge transfer mechanism, the suspended semiconductor particle photocatalyst can be regarded as a short-circuited PEC cell [11, 12].

In 1978, Halmann found that CO_2 dissolved in the electrolyte could be reduced to formic acid (HCOOH), formaldehyde, and methanol (CH_3OH) by using p-GaP single crystal, carbon rod, and K_2HPO_4–KH_2PO_4 buffer solution as cathode, anode, and electrolyte, respectively, under the necessary applied bias voltage [13].

In the same year, Somorjai first used $SrTiO_3$ to achieve the photocatalytic conversion of CO_2 and water vapor to CH_4 [14].

In 1979, Inoue et al. [15] systematically reported that WO_3, TiO_2, ZnO, CdS, GaP, SiC, and other semiconductor catalysts suspend in the saturated aqueous solution of CO_2 could achieve the photoreduction of CO_2 to HCOOH, formaldehyde (HCHO), CH_3OH, and CH_4 under the illumination of xenon lamp and high-pressure mercury lamp. More importantly, the reaction mechanism of CO_2 photoreduction was proposed.

In 1980, Kawai and Sakata reported that H_2 was produced by photocatalytic reforming biomass and its derivatives (glycine, glutamic acid, proline, white gelatin protein) in water using Pt/RuO_2/TiO_2 photocatalyst. Only H_2 and CO_2 products were released from the photocatalytic processes [16].

Sequentially, Pt/TiO_2 [17] and (Pt) $SrTiO_3$ [18, 19] have also been proved to exhibit good photocatalytic activity for the decomposition of water into H_2. Therefore, since the early 1980s, heterogeneous photocatalysis technology has gradually formed two main research directions: environmental photocatalysis and energy photocatalysis.

Along with the two main research directions, researchers from the fields of physics, chemistry, materials science, and environmental science have made a series of remarkable achievements in developing new semiconductor materials, revealing the mechanism of photocatalysis process and improving the quantum efficiency of photocatalysis reaction. Table 1.1 systematically summarizes a series of notable advances in the development of efficient heterogeneous photocatalysts. As seen from Table 1.1, among various kinds of photocatalysts, TiO_2-based photocatalysts were undoubtedly the most studied, because TiO_2 has many advantages, such as low cost, nontoxicity, strong oxidation–reduction ability, light and chemical corrosion resistance, and excellent stability. However, it remains a great challenge to design and develop high-performance TiO_2-based photocatalytic materials. The key problems lie in how to enhance the quantum efficiency of TiO_2 photocatalysis, promote the separation of photogenerated charge carriers, and expand the visible light response range. So far, TiO_2 modification methods have been widely developed, such as dye and quantum dot (QD) sensitization [30]; cocatalyst loading [17, 21–23, 70, 73, 74]; metal and non-metal ion doping [31, 37, 39, 40]; reasonable control of defects and exposed crystal facets [57, 66, 67]; nanostructure modification (including the construction of colloidal nanocrystals, hierarchical structures, hollow microspheres, and nanosheet structures) [29, 44, 45, 52, 53, 77]; formation of

Table 1.1 Some crucial advances in the development of efficient heterogeneous photocatalysts.

No.	Photocatalysts	Highlights	Group	References (year)
1	TiO_2 photoelectrode	The discovery of Fujishima–Honda effect of TiO_2	Fujishima and Honda	[3] (1972)
2	TiO_2 powders	Photodechlorination of polychlorinated biphenyls	Carey	[4] (1976)
3	TiO_2 powders	Photocatalytic oxidation of CN^- in aqueous solutions	Bard	[5] (1977)
4	TiO_2 powders	Overall water splitting on TiO_2 consisting of mixtures of anatase and rutile	Schrauzer	[6] (1977)
5	Pt–TiO_2 particle systems	Bard's concept, "a short-circuited photoelectrochemical cell"	Bard	[9, 11, 12, 20] (1978)
6	P-type GaP photocathode	Photo-assisted electrolytic reduction of CO_2 in aqueous phase	Halmann	[13] (1978)
7	TiO_2, CdS, and SiC powders	Photocatalytic reduction of carbon dioxide in aqueous suspensions of semiconductor powders	Inoue	[15] (1979)
8	Pt/TiO_2 powders	Decompose H_2O into H_2 and O_2 under UV irradiation	Sato and White	[17, 21] (1980)
9	RuO_2/TiO_2/Pt powders	Photocatalytic reforming of carbohydrates into hydrogen	Kawai	[16] (1980)
10	Platinized or Pt-free $SrTiO_3$ single crystals	Production of H_2	Wagner	[18, 19] (1980)
11	Pt and RuO_2 co-loaded TiO_2 sol	First report on the photocatalytic water decomposition by loading dual cocatalysts (with a quantum yield of $30 \pm 10\%$)	Grätzel	[22, 23] (1981)
12	$SrTiO_3$–NiO	The utilization of NiO as H_2-evolution cocatalysts	Domen	[24] (1982)
13	CdS–TiO_2	Improved photocatalytic efficiency through inter-particle electron transfer	Grätzel	[25] (1984)
14	$Zn_xCd_{1-x}S$ solid solutions	The utilization of solid solutions for H_2 evolution	White	[26] (1985)
15	$SrTiO_3$–Ni@NiO	The utilization of Ni@NiO core/shell H_2-evolution cocatalysts	Domen	[27, 28] (1986)
16	TiO_2 particles	Size quantization effects of small-particle titania	Anpo	[29] (1987)
17	Colloidal TiO_2 films	TiO_2-based solar cells sensitized by Ru-based dyes	Grätzel	[30] (1991)
18	TiO_2 colloids	Metal ion-doped quantum-sized (2–4 nm) TiO_2 colloids	Hoffmann	[31] (1994)
19	TiO_2 polycrystalline film	Light-induced amphiphilic surface of TiO_2	Fujishima	[32] (1997)

Table 1.1 (Continued)

No.	Photocatalysts	Highlights	Group	References (year)
20	$BiVO_4$ particles	First report on the $BiVO_4$ photocatalyst	Kudo	[33, 34] (1998)
21	$In_{1-x}Ni_xTaO_4$ ($x = 0$–0.2) solid solutions	Ni-doped indium–tantalum oxide	Zou	[35] (2001)
22	(WO_3 or Fe_2O_3)/dye-sensitized TiO_2	First report on the concept of "direct Z-scheme"	Grätzel	[36] (2001)
23	TiO_2 films/powders	First report on N-doped TiO_2	Asahi	[37] (2001)
24	Pt-loaded anatase TiO_2 and rutile TiO_2	The Z-scheme water splitting using IO_3^-/I^- redox mediator	Arakawa	[38] (2001)
25	TiO_2 photoelectrodes	First report on C-doped TiO_2	Khan	[39] (2002)
26	TiO_2 powders	First report on F-doped TiO_2	Yu	[40] (2002)
27	Ta_3N_5	First report on the Ta_3N_5 photocatalyst	Domen	[41] (2002)
28	TaON	First report on the TaON photocatalyst	Domen	[42] (2002)
29	$AgInZn_7S_9$	$AgInZn_7S_9$ solid solution photocatalyst for H_2 evolution	Kudo	[43] (2002)
30	Hierarchical TiO_2	First application of hierarchical TiO_2 in photocatalysis	Yu	[44, 45] (2003)
31	$NiO/NaTaO_3$:La photocatalyst	An apparent quantum yield of 56% at 270 nm	Kudo	[46] (2003)
32	$(AgIn)_xZn_{2(1-x)}S_2$ solid solution (Pt-loaded)	An apparent quantum yield of 20% for H_2 evolution at 420 nm	Kudo	[47] (2004)
33	GaN:ZnO solid solutions	Overall water splitting on $(Ga_{1-x}Zn_x)(N_{1-x}O_x)$ solid solution photocatalyst	Domen	[48–50] (2005)
34	CdS–Au–TiO_2 nanojunctions	All-solid-state Z-scheme system	Tada	[51] (2006)
35	Mesoporous anatase hollow microspheres	Fabrication of hollow TiO_2 microspheres by chemically induced self-transformation	Yu	[52, 53] (2006)
36	BiOX powders	First report on the BiOX (X = Cl, Br, I) photocatalysts	Zhang	[54] (2008)
37	TiO_2–graphene composites	The photocatalytic reduction of graphene oxide using TiO_2	Kamat	[55] (2008)
38	Au–TiO_2	The concept of plasmonic photocatalysts	Tatsuma	[56] (2005)

(*continued*)

Table 1.1 (Continued)

No.	Photocatalysts	Highlights	Group	References (year)
39	TiO_2 nanosheets	The fabrication of anatase TiO_2 crystals predominantly exposed with (101) facets	Lu and Qiao	[57] (2008)
40	MoS_2/CdS	The utilization of MoS_2 as H_2-evolution cocatalysts	Li	[58] (2008)
41	g-C_3N_4	First report on the g-C_3N_4 photocatalyst	Wang	[59] (2009)
42	Pt–PdS/CdS	The highest quantum efficiency of H_2 generation (93%) by loading Pt and PdS as dual cocatalysts on CdS	Li	[60] (2009)
43	CdS–ZnO	Demonstrated ZnO/CdS heterostructures based on the Z-scheme mechanism	Lu and Cheng	[61] (2009)
44	(Pt/ZrO_2/TaON)–(Pt/WO_3)	The highest quantum yield of 6.3% for Z-scheme systems	Domen	[62] (2010)
45	CdS–NiS	The utilization of NiS as H_2-evolution cocatalysts	Xu	[63] (2010)
46	Cu and Pt co-loaded TiO_2 nanotube arrays	Photocatalytic conversion of CO_2 and water vapor into hydrocarbon fuels	Grimes	[64] (2009)
47	Ag_3PO_4	First report on the Ag_3PO_4 photocatalyst	Ye	[65] (2010)
48	Hollow TiO_2 microspheres and photocatalytic selectivity	Tunable photocatalytic selectivity by using exposed (001) facets and designed surface chemistry	Yu	[66] (2010)
49	TiO_2 nanocrystals	First report on black hydrogenated TiO_2	Chen	[67] (2011)
50	CdS cluster/graphene composite	Photocatalytic H_2 evolution over graphene-based composite semiconductor	Yu	[68] (2011)
51	$BiVO_4$–(Ru/$SrTiO_3$:Rh)	Construction of all-solid-state Z-scheme systems by using rGO as a solid-state electron mediator	Amal	[69] (2011)
52	$Cu(OH)_2$ cluster modified TiO_2	Utilization of $Cu(OH)_2$ as H_2-evolution cocatalysts	Yu	[70] (2011)
53	$Ni(OH)_2$ cluster modified TiO_2	Enhanced photocatalytic H_2 production activity of TiO_2 by $Ni(OH)_2$ cluster modification	Yu	[71] (2011)
54	CuS/ZnS porous nanosheet photocatalysts	A visible light-induced interfacial charge transfer (IFCT) mechanism for enhanced photocatalysis	Yu	[72] (2011)
55	Ultrafine Pt-loaded TiO_2 single crystals	CO_2 photoreduction to CH_4 with a super high yield of 1361 μmol g-cat^{-1} h^{-1}	Biswas	[73] (2012)

Table 1.1 (Continued)

No.	Photocatalysts	Highlights	Group	References (year)
56	(MoS_2 + graphene)/TiO_2 composites	2D–2D hybrid of MoS_2 and graphene as dual-electron cocatalysts for H_2 evolution	Yu	[74] (2012)
57	rGO–$Zn_xCd_{1-x}S$ nanocomposites	Noble metal-free photocatalysts for enhanced solar photocatalytic H_2 Production	Yu	[75] (2012)
58	Direct Z-scheme g-C_3N_4/TiO_2	Enhanced photocatalytic performance of direct Z-scheme g-C_3N_4/TiO_2 photocatalyst for decomposition of formaldehyde in air	Yu	[76] (2013)
59	Surface heterojunction	Surface heterojunction within single TiO_2 particles	Yu	[77] (2014)
60	Ternary NiS/$Zn_xCd_{1-x}S$/rGO nanocomposites	Co-loading of noble metal-free reduced graphite oxide (rGO) and NiS (reduction and oxidation cocatalysts) on $Zn_xCd_{1-x}S$	Yu	[78] (2014)
61	Carbon nanodot–C_3N_4	Overall water splitting by the metal-free photocatalysts	Kang	[79] (2015)
62	Hierarchical CdS–WO_3 heterostructure	A direct hierarchical Z-scheme CdS–WO_3 heterostructure for photocatalytic CO_2 reduction to CH_4	Yu	[80] (2015)
63	MS_2–CdS (M = W or Mo) nanohybrids	Wurtzite CdS nanocrystals hybridized with single-layer MS_2 nanosheets for efficient photocatalytic H_2 evolution	Zhang	[81] (2015)
64	1D poly(diphenylbutadiyne) (PDPB) nanostructures	Metal-free PDPB nanofibers for photocatalytic degradation of methyl orange and phenol	Remita	[82] (2015)
65	Graphene-g-C_3N_4 nanocomposites	Sandwich-like graphene-g-C_3N_4 hybrid nanostructures for enhanced visible light photoreduction of CO_2 to CH_4	Chai	[83] (2015)
66	g-C_3N_4/ZnO binary nanocomposite	A direct Z-scheme g-C_3N_4/ZnO system for photocatalytic reduction of CO_2 to CH_3OH	Peng	[84] (2015)
67	Ultrathin g-C_3N_4 nanosheet assemblies	Hierarchical amine-functionalized ultrathin g-C_3N_4 nanosheet assemblies for photoreduction of CO_2 to CH_4 and CH_3OH	Yu	[85] (2016)
68	Hybrid film of g-C_3N_4 and Ti_3C_2 nanosheets	Ti_3C_2 (with MXene phase) nanosheets as cocatalyst for photocatalytic O_2 evolution	Qiao	[86] (2016)
69	$SrTiO_3$:La, Rh, and $BiVO_4$:Mo powders embedded into an Au layer	Z-scheme systems for pure water (pH 6.8) splitting with a solar-to-hydrogen energy conversion efficiency of 1.1% and an apparent quantum yield of over 30% at 419 nm	Domen	[87] (2016)

(*continued*)

Table 1.1 (Continued)

No.	Photocatalysts	Highlights	Group	References (year)
70	FeCoW oxyhydroxides	Report on the lowest overpotential (191 mV) for the oxygen evolution reaction	Sargent and Vojvodic	[88] (2016)
71	Hollow cobalt-based bimetallic sulfide	Hollow $Zn_{0.30}Co_{2.70}S_4$ with higher electrocatalytic HER activity than most noble metal-free electrocatalysts	Zou	[89] (2016)
72	GaAs/InGaP/TiO_2/Ni photoanode, Pd/C/Ti mesh cathode	Solar-driven reduction of 1 atm of CO_2 to formate at 10% energy conversion efficiency	Lewis	[90] (2016)
73	Hierarchical g-C_3N_4 nanostructures	Hierarchical porous O-doped g-C_3N_4 nanotubes for photocatalytic CO_2 reduction to CH_3OH	Yu	[91] (2017)
74	Au/$La_2Ti_2O_7$ sensitized with black phosphorus	An efficient broadband solar-responsive photocatalyst for H_2 production	Majima	[92] (2017)
75	Black phosphorus nanosheets	Visible light photocatalytic H_2 evolution of black phosphorus nanosheets	Yang and Du	[93] (2017)
76	Ti_3C_2/CdS nanocomposites	Ti_3C_2 MXene cocatalysts significantly boosting photocatalytic H_2 production activity over CdS	Qiao	[94] (2017)
77	Ni/CdS nanoparticles	Photocatalytic H_2 evolution by dehydrogenation of 2-propanol	Xiao	[95] (2016)
78	In-plane (Cring)–g-C_3N_4 heterostructure	2D g-C_3N_4-based in-plane heterostructures for efficient photocatalytic H_2 production	Liu and Wei	[96] (2017)
79	$W_{18}O_{49}$/g-C_3N_4 heterostructure	First report on the non-metal plasmonic $W_{18}O_{49}$	Dong	[97] (2017)
80	Defective TiO_2	Photocatalytic NH_3 production from water and N_2 at atmospheric pressure and room temperature over surface oxygen vacancies of TiO_2	Shiraishi	[98] (2017)
81	Defective one-unit-cell $ZnIn_2S_4$ atomic layers	Defect-mediated electron–hole separation in one-unit-cell $ZnIn_2S_4$ layers for boosted solar-driven CO_2 reduction	Xie	[99] (2017)
82	$CsPbBr_3$ QD/GO	A $CsPbBr_3$ perovskite quantum dot/graphene oxide composite for photocatalytic CO_2 reduction	Kuang	[100] (2017)
83	Methylammonium lead iodide ($MAPbI_3$)	Photocatalytic H_2 generation from hydriodic acid using methylammonium lead iodide	Nam	[101] (2017)

Table 1.1 (Continued)

No.	Photocatalysts	Highlights	Group	References (year)
84	Black phosphorus/ g-C_3N_4	Metal-free photocatalyst for H_2 evolution in visible to near-infrared region	Majima	[102] (2017)
85	NiS/Ni/g-C_3N_4	Constructing Ni interface layers in the g-C_3N_4 nanosheets/amorphous NiS heterojunctions for efficient photocatalytic H_2 generation	Li	[103] (2017)
86	(Au/CoO_x–$BiVO_4$)/(ZrO_2/TaON)	Photocatalytic Z-scheme overall water splitting system with an apparent quantum efficiency of 10.3% at 420 nm	Zhang and Li	[104] (2018)
87	β-ketoenamine COFs	Diacetylene-functionalized covalent organic framework (COF) for photocatalytic hydrogen generation	Thomas	[105] (2018)
88	High-symmetry Cu_2O photocatalyst particle	Demonstrating that the holes and electrons are transferred to the illuminated and shadow regions of a single Cu_2O particle, respectively	Li	[106] (2018)
89	Ni_3C/CdS	Ni_3C nanoparticles as a new cocatalyst for photocatalytic H_2 evolution	Li	[107] (2018)
90	P-doped CdS	P-doped CdS for photocatalytic water splitting without sacrificial agents	Chen	[108] (2018)
91	Graphdiyne/TiO_2 nanofibers	Graphdiyne as a new photocatalytic CO_2 reduction cocatalyst	Yu	[109] (2019)
92	WO_3/g-C_3N_4	Firstly proposing the concept of step-scheme (S-scheme) heterojunction	Yu	[110] (2019)
93	TiO_2/CdS	The direct Z-scheme charge carrier migration pathway firstly confirmed by *in situ* irradiated X-ray photoelectron spectroscopy	Yu	[111] (2019)
94	C_3N_5	First report of a C_3N_5 photocatalyst	Kumar, and Shankar	[112] (2019)
95	Atomically thin $CuIn_5S_8$ layers	Selective visible light-driven photocatalytic CO_2 reduction to CH_4 mediated by atomically thin $CuIn_5S_8$ layers	Xie	[113] (2019)
96	Single-atom Cu/TiO_2 photocatalysts	Reversible and cooperative photoactivation	Hyeon, Kim, and Nam	[114] (2019)
97	Resorcinol–formaldehyde resins	Metal-free semiconductor photocatalysts for solar-to-hydrogen peroxide energy conversion	Shiraishi	[115] (2019)
98	$Y_2Ti_2O_5S_2$	Oxysulfide photocatalyst for visible light-driven overall water splitting	Domen	[116] (2019)
99	Al-doped $SrTiO_3$	Achieving the upper limit of quantum efficiency for overall water splitting	Domen	[117] (2020)

heterojunctions (by coupling with other semiconductors and nanocarbon materials) [55, 74]; etc. The following are some examples.

In 2001, the doping of N into TiO_2 (by replacing O in the lattice) [37] was first reported in the journal *Science*. The resulting $TiO_{2-x}N_x$ material showed high photocatalytic activity under the visible light ($\lambda < 500$ nm). The publication of this work started the research of the second-generation TiO_2 photocatalysts. Subsequently, the visible photocatalytic properties of S-, F-, and C-doped TiO_2 have been reported successively [39, 40]. Although these studies have greatly improved the light absorption of photocatalytic materials in the visible light region, the introduced modifiers, N or C atoms, are easy to disintegrate from the crystal lattice under the light irradiation. Therefore, the stability of these modified visible light photocatalytic materials is poor, and the reusability in practical application is limited to a certain extent [118].

In 2008, Yang and Qiao successfully synthesized TiO_2 nanoflakes with high exposure ratio of (001) crystal facets by using hydrogen fluride (HF) as crystal surface control agent [57]. Further studies showed that TiO_2 hollow nanospheres with high exposure ratio of the (001) crystal facets and surface fluorination had better photocatalytic degradation activity and good selectivity for methyl orange [66]. More interestingly, Yu et al. proposed the concept of surface (crystal surface) heterojunction [77]. By optimizing the ratio of different exposed crystal facets of TiO_2, the best photocatalytic activity for CO_2 reduction to CH_4 was achieved [77].

In 2003, Zhang and Yu constructed the hierarchical porous TiO_2 microspheres and confirmed that the hierarchical mesoporous and macroporous structures can effectively increase the photocatalytic degradation activity of *n*-pentane in the gas phase [44, 45]. Meanwhile, Yu et al. synthesized the mesoporous hollow TiO_2 microspheres by using a chemical-induced self-transformation strategy, whose photocatalytic activity was double that of P25 [53].

In 2011, Chen et al. first developed black TiO_2 with disordered surface structure and confirmed its high hydrogen production activity [67]. This study further stimulated the researchers to control the defects and surface structure of the photocatalysts, so as to improve the photocatalytic activity. In addition, various noble metal and non-noble metal cocatalysts (such as Pt, $Cu(OH)_2$, NiO, MoS_2, and graphene) have been widely developed and applied to greatly enhance the H_2 production and CO_2 reduction activities of TiO_2-based photocatalysts [22, 23, 27, 28, 64, 73, 74]. All in all, as the core photocatalyst, TiO_2 modification research and diversified applications will continue in full swing.

In addition to TiO_2-based photocatalysts, the development of non-TiO_2-based photocatalysts and the exploration of new mechanisms have been the recent focus of photocatalytic research. Since the 1980s, a variety of new non-TiO_2-based photocatalysts have been found, such as $SrTiO_3$ [18, 19], $Zn_xCd_{1-x}S$ [26], $BiVO_4$ [33, 34], $In_{1-x}Ni_xTaO_4$ [35], Ta_3N_5 [41], TaON [42], $AgInZn_7S_9$ [43], $(AgIn)_xZn_{2(1-x)}S_2$ [47], $(Ga_{1-x}Zn_x)(N_{1-x}O_x)$ [48–50], BiOX (X = Cl, Br, I) [54], Ag@AgCl [119], g-C_3N_4 [59, 120], C_3N_5 [112], resorcinol–formaldehyde resins [115], β-ketoenamine covalent organic frameworks (COFs) [105], $Y_2Ti_2O_5S_2$ [116], Ag_3PO_4 [65], etc. There is no doubt that g-C_3N_4 has become a dazzling new star in the field of photocatalysis in recent years [120–123]. Importantly, the appearance of graphene, a new type

of two-dimensional (2D) ultrathin and highly conductive material, has injected infinite power into the design and development of new efficient photocatalysts. Various kinds of graphene-based composite photocatalyst materials are springing up [68, 74, 75, 124–127]. On the other hand, new photocatalytic mechanisms have been studied constantly. Bard first proposed the Z-scheme photocatalytic mechanism of biomimetic photosynthesis in 1979 [20]. In 2001, Arakawa and coworkers successfully constructed the first Z-scheme photocatalytic overall water splitting system with I^-/IO_3^- redox pairs, Pt-loaded rutile TiO_2 (H_2 production catalyst), and anatase TiO_2 (O_2 production catalyst) [38]. Domen achieved a quantum efficiency of 6.3% for photocatalytic overall water splitting under monochromatic light irradiation ($\lambda = 420.5$ nm), by using $Pt/ZrO_2/TaON$, Pt/WO_3, and I^-/IO_3^- as the H_2 production photocatalyst, O_2 production photocatalyst, and the electron mediator, respectively [62]. More recently, Zhang and Li reported a photocatalytic Z-scheme overall water splitting system with an apparent quantum efficiency (AQE) of 10.3% at 420 nm using $[Fe(CN)_6]^{3-}/[Fe(CN)_6]^{4-}$, $Au/CoO_x–BiVO_4$, and $ZrO_2/TaON$ as redox mediator, H_2-evolving, and O_2-evolving photocatalysts, respectively, which is so far the Z-scheme reaction system with the highest quantum efficiency for photocatalytic overall water splitting [104]. At the same time, all-solid-state and direct Z-scheme systems have been successfully developed and applied to photocatalytic decomposition of water and reduction of CO_2 [51, 69, 80, 84, 111, 128–130]. Moreover, a photoinduced interfacial charge transfer (IFCT) mechanism has been proved to be useful in the design and construction of novel visible light photocatalysts [72]. In particular, recently reported black phosphorus [92, 93], MXene cocatalyst [86, 94], graphdiyne [109], defective one-unit-cell $ZnIn_2S_4$ atomic layers [99], atomically thin $CuIn_5S_8$ layers [113], planar heterojunction [96], and van der Waals heterojunction [131, 132] provide a broader space for the design of 2D semiconductor photocatalysts. In addition, some other efficient hydrogen production systems such as Pt–PdS/CdS [60], non-noble metal (MoS_2/CdS [58], graphene/$Zn_xCd_{1-x}S$ [75], NiS/$Zn_xCd_{1-x}S$/graphene [78], Ni_3C/CdS [107], CdS–NiS [63], NiS/Ni/g-C_3N_4 [103], and C_3N_4–CdS–NiS [133]) as well as metal-free carbon dots/g-C_3N_4 [79] have been successfully constructed successively. All in all, the development of a series of non-TiO_2-based heterojunction photocatalytic materials, new mechanisms, and efficient systems will continue to advance the research in the field of photocatalysis.

1.3 Fundamental Principles of Solar Energy Photocatalysis

1.3.1 Basic Mechanisms for Solar Energy Photocatalysis

So far, four basic mechanisms have been extensively employed to describe the charge carrier generation and migration processes in heterogeneous photocatalysis, namely, inorganic semiconductor photocatalysis (Figure 1.2a), organic semiconductor photocatalysis (Figure 1.2b), surface plasmon resonance (SPR, Figure 1.2c), and

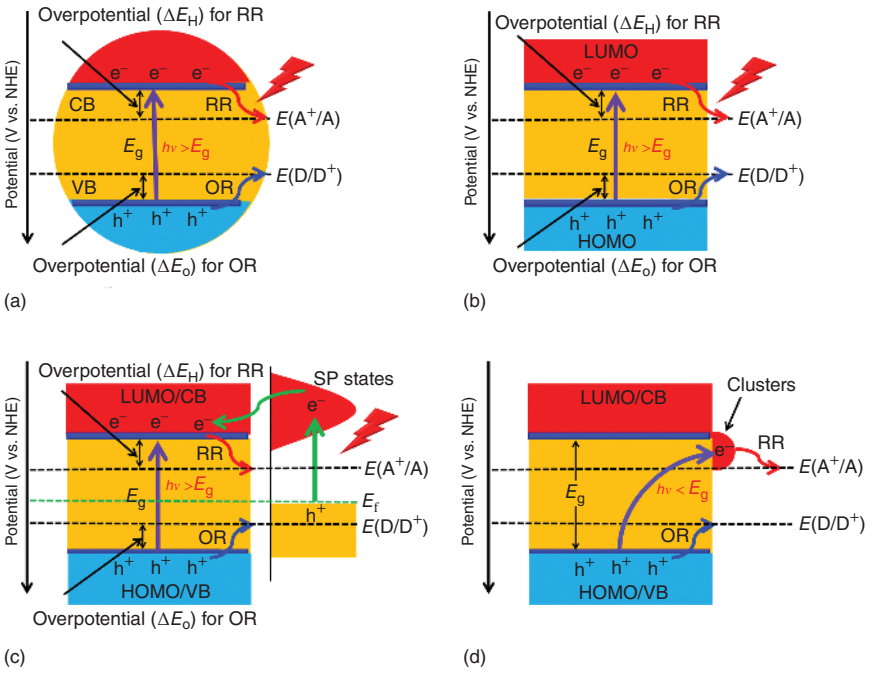

Figure 1.2 Photocatalytic mechanisms for (a) inorganic (TiO_2, CdS, WO_3, ZnO, $BiVO_4$, Si, etc.) and (b) organic (dyes, complexes, polymers, g-C_3N_4, etc.) semiconductors, (c) surface plasmon resonance (SPR) (Au, Ag, Cu, Bi, etc.), and (d) interfacial charge transfer (IFCT) (Cu(II), Fe(III), clusters, etc.). Source: Li et al. [134].

IFCT (Figure 1.2d). Among these four basic photocatalytic mechanisms, inorganic semiconductor photocatalysis and organic semiconductor photocatalysis are the most commonly used mechanisms for heterogeneous photocatalysis, and they share the similar principles. Typically, the electrons in the ground-state valence band (VB) or highest occupied molecular orbital (HOMO) could be photoexcited into the vacant conduction band (CB) or lowest unoccupied molecular orbital (LUMO) by absorption of the suitable incident photons. As a result, the separated photoinduced electrons and holes in CB/LUMO and VB/HOMO can rapidly migrate to the surface of the semiconductors and initiate the reduction and oxidation reactions, respectively. Clearly, the heterogeneous photocatalysis over the traditional inorganic semiconductors (i.e. TiO_2 [135], ZnO, WO_3 [136], CdS [107, 126, 137], and $BiVO_4$ [138]) and organic semiconductors (i.e. dyes [139], complexes [140–143], polymers [82, 144–147], graphene oxide [148], and g-C_3N_4 [120–123]) could be well explained by these two mechanisms, respectively. Notably, the photocatalytic activity for these two kinds of semiconductors could be further enhanced by different modification strategies, such as heteroatom doping, molecular doping and their co-doping, and vacancy creation [120, 149–152]. The third photocatalytic mechanism is the SPR, as shown in Figure 1.2c, which widely exists in the nanostructured noble metals (mainly Au and Ag), non-noble metal plasmonic metals (i.e. Bi and Cu) [153–161], and non-metal plasmonic materials. The plasmonic photocatalysis observed in

the systems with contacted and separated semiconductors could be explained by SPR-mediated charge injection [162–173] and the near-field electromagnetic and scattering mechanisms [163, 174], respectively. On one hand, it is expected that regulation of composition, morphology, and structure of the metals can be used to further enhance the plasmonic photocatalysis. On the other hand, more and more novel plasmonic materials are expected to be exploited in the near future. Additionally, in some cases, it was found that some semiconductors can be excited by the incident photons with energy smaller than their corresponding bandgap energies, which could be well explained by the IFCT mechanism (Figure 1.2d). Creutz et al. first theoretically proposed the IFCT initiated by visible light in 2006 [175]. So far, the IFCT mechanism has been successfully used to explain the photocatalytic O_2 reduction or H_2 evolution over several clusters or chemical bonds (i.e. CuS, Cr_xO_y, Ag, Cu(II), and Fe(III)) that are modified wide band semiconductors. Clearly, these previously mentioned four mechanisms could be responsible for various kinds of heterogeneous photocatalysis reactions.

1.3.2 Thermodynamic Requirements for Solar Energy Photocatalysis

The energy band structure of a given semiconductor essentially determines the thermodynamic characteristics and largely affects the photocatalytic performance of the material. According to the theory of solid energy band, the electronic energy levels near the Fermi level of a semiconductor are separated, while they are continuous in bulk metal conductors. The band structure is generally composed of a low-energy VB (composed of electron filled orbits) and a high-energy CB (composed of an empty orbits). The energy gap between the VB and CB is the bandgap, expressed as E_g. The bandgap width of a given semiconductor determines its optical absorption performance. The relationship between the absorption wavelength threshold λ_g and the E_g of a semiconductor can be described by Eq. (1.1). It can be seen from the equation that the bandgap width of a semiconductor directly affects the light utilization for photocatalytic reactions. The wider the bandgap of a semiconductor is, the higher the energy of the photons it can absorb. These photons with higher energy correspond to shorter wavelength, and thus a semiconductor with a wider bandgap typically exhibits narrower absorption range, which is mainly concentrated in the UV region of the solar spectrum. In contrast, the narrower the bandgap is, the lower the energy of the photons a semiconductor can absorb, which corresponds to longer wavelength, indicating that the semiconductor can use more visible light in the solar spectrum. Because the visible light accounts for about 43% of the solar light, the development of narrow bandgap semiconductors and the broadening of the light response range of photocatalysts have become the focus of research.

$$\lambda_g = 1240/E_g(\text{eV}) \tag{1.1}$$

When the energy of the incident light equals or exceeds the bandgap energy of a semiconductor, the semiconductor can absorb the incident photons and excite electrons from the VB to the CB. The photogenerated electrons and holes could drive the reduction and oxidation reactions, respectively, which can lead to the redox reactions

similar to those in the electrolysis process. In thermodynamics, the width of bandgap determines the absorption ability of a given semiconductor photocatalyst to photons, while the CB and VB positions of a semiconductor determine the possibility of photocatalysis. Therefore, the band structure (mainly the width of bandgap, the positions of CB and VB) and the redox potential of the adsorbed species essentially determine the light absorption capacity, the possibility of photocatalytic reaction, and the strength of the thermodynamic driving force.

From the thermodynamic viewpoint, to accomplish the photocatalytic reactions, the redox potentials for the surface reduction and oxidation half reactions should match well with the semiconductors' CB and VB levels, respectively. The standard redox potentials of several half reactions have been summarized in Table 1.2 [121, 127, 176]. Notably, the redox potential of almost all these reactions exhibit the same linear pH dependence ($V_{pH} = V_{pH(0)} - 0.059$ pH), except for that of pH-independent single-electron O_2 reduction ($E^0(O_2/O_2^-)$) [176, 177]. The reduction and oxidation half reactions in different photocatalytic systems are highlighted in Figure 1.3. Clearly, hydrogen evolution reaction (HER), CO_2 reduction reaction (CRR), and oxygen reduction reaction (ORR) are the three basic reduction half reactions for the different photocatalytic systems. The four-electron oxygen evolution reaction (OER), which is crucial for achieving solar fuel production (via overall water splitting and CO_2 reduction), is more challenging, due to its large overpotential and sluggish kinetics. Therefore, any factor that boosts the efficiency of these half reactions is beneficial for the enhancement of photocatalytic activity. The relative positions between band levels (at pH = 7 in aqueous solution) for some commonly used semiconductor photocatalysts relative to the redox potentials of typical half reactions and their potential applications are listed in Figure 1.4. Clearly, on one hand, the sufficiently positive VB potentials for some oxidative semiconductors (e.g. WO_3, ZnO, SnO_2, $SrTiO_3$, $BiVO_4$, Bi_2WO_6, BiOCl, and BiOBr) could drive the production of the $^{\cdot}OH$ radicals (on the left side of Figure 1.4), thus leading to their promising applications in the photodegradation of organic pollutants. On the other hand, more negative CB positions in some reductive photocatalysts (e.g. Ta_3N_5, TaON, CdS, g-C_3N_4, SiC, ZnS, BiOCl, Si, Bi_2S_3, and Cu_2O) could efficiently achieve the photocatalytic H_2 evolution and CO_2 reduction. It is noted that several semiconductors (e.g. Ta_3N_5, TaON, CdS, g-C_3N_4, SiC, ZnS, BiOCl, $SrTiO_3$, ZnO, and TiO_2) with suitable CB and VB positions for both H_2 and O_2 evolution are promising candidates for photocatalytic overall water splitting.

1.3.3 Dynamics Requirements for Solar Energy Photocatalysis

Thermodynamically speaking, the suitable band structure is necessary for semiconductor materials to drive the photocatalytic redox reactions, but it is not a sufficient condition for achieving the photocatalytic redox activity. This is because, in the process of photocatalysis, there are many dynamic factors that will affect the observed activity of a given photocatalyst. Generally, the overall photocatalytic quantum efficiency was significantly related to the kinetics of four successive kinetic processes: light harvesting, charge separation, charge carrier migration/transport, and surface

Table 1.2 Standard redox potentials for selected species.

Reaction	$E^{\circ\prime}$ (V) vs. NHE at pH 0
H_2	
$2H^+ + 2e^- \rightarrow H_2(g)$	0
O_2 and N_2	
$O_2(g) + e^- \rightarrow O_2^{-\bullet}(aq)$	−0.33
$O_2(g) + H_2O + 2e^- \rightarrow HO_2^-(aq) + OH^-$	−0.0649[a)]
$O_2(g) + H^+ + e^- \rightarrow HO_2^{\bullet}(aq)$	−0.046
$HO_2^-(aq) + H_2O + e^- \rightarrow {}^{\bullet}OH + 2OH^-$	0.184[a)]
$O_2^{-\bullet}(aq) + H_2O + e^- \rightarrow HO_2^-(aq) + OH^-$	0.2[a)]
$O_2(g) + 2H^+ + 2e^- \rightarrow H_2O_2(aq)$	0.695
$2H_2O(aq) + 4h^+ \rightarrow O_2(g) + 4H^+$	1.229
$OH^- + h^+ \rightarrow {}^{\bullet}OH$	2.69
$4OH^-(aq) + 4h^+ \rightarrow O_2(g) + 2H_2O$	0.401
$N_2(g) + 2H_2O + 6H^+ + 6e^- \rightarrow 2NH_4OH(aq)$	0.092
$O_3(g) + 2H^+ + 2e^- \rightarrow O_2(g) + H_2O$	2.075
Metal ion	
$MoO_4^{2-} + 4H_2O + 6e^- \rightarrow Mo(s) + 8OH^-$	−0.913[a)]
$Co(OH)_2 + 2e^- \rightarrow Co(s) + 2OH^-$	−0.733[a)]
$Ni(OH)_2 + 2e^- \rightarrow Ni(s) + 2OH^-$	−0.72[a)]
$Cu_2O(s) + H_2O + 2e^- \rightarrow 2Cu(s) + 2OH^-$	−0.365[a)]
$Co^{2+} + 2e^- \rightarrow Co(s)$	−0.277
$Ni^{2+} + 2e^- \rightarrow Ni(s)$	−0.257
$Mo^{3+} + 3e^- \rightarrow Mo(s)$	−0.2
$AgI + e^- \rightarrow Ag(s) + I^-$	−0.1522
$AgBr + e^- \rightarrow Ag(s) + Br^-$	0.0711
$AgCl + e^- \rightarrow Ag(s) + Cl^-$	0.2223
$Sn^{4+} + 2e^- \rightarrow Sn^{2+}$	0.15
$Cu^{2+} + e^- \rightarrow Cu^+$	0.159
$BiOCl + 2H^+ + 3e^- \rightarrow Bi(s) + H_2O + Cl^-$	0.1697
$Bi^{3+} + 3e^- \rightarrow Bi(s)$	0.308
$Cu^{2+} + 2e^- \rightarrow Cu(s)$	0.340
$Cu^+ + e^- \rightarrow Cu(s)$	0.520
$PdCl_4^{2-} + 2e^- \rightarrow Pd(s) + 4Cl^-$	0.64
$PtCl_4^{2-} + 2e^- \rightarrow Pt(s) + 4Cl^-$	0.758
$Rh^{3+} + 3e^- \rightarrow Rh(s)$	0.76
$Fe^{3+} + e^- \rightarrow Fe^{2+}$	0.771

(*continued*)

Table 1.2 (Continued)

Reaction	$E°'$ (V) vs. NHE at pH 0
$Ag^+ + e^- \rightarrow Ag(s)$	0.7991
$IrCl_6^{3-} + 3e^- \rightarrow Ir(s) + 6Cl^-$	0.86
$Pd^{2+} + 2e^- \rightarrow Pd(s)$	0.915
$[AuCl_4]^- + 3e^- \rightarrow Au(s) + 4Cl^-$	0.93
$NiO_2 + 4H^+ + 2e^- \rightarrow Ni^{2+} + 2H_2O$	1.593
CO_2	
$CO_2 + e^- \rightarrow CO_2^-$	−1.9
$2CO_2(g) + 2H^+ + 2e^- \rightarrow HOOCCOOH(aq)$	−0.481
$CO_2(g) + 2H^+ + 2e^- \rightarrow HCOOH(aq)$	−0.199
$CO_2(g) + 2H^+ + 2e^- \rightarrow CO(g) + H_2O$	−0.11
$CO_2 + 4H^+ + 4e^- \rightarrow C + 2H_2O$	0.206
$CO_2 + 4H^+ + 4e^- \rightarrow HCHO + H_2O$	−0.07
$CO_2 + 6H^+ + 6e^- \rightarrow CH_3OH + H_2O$	0.03
$CO_2 + 8H^+ + 8e^- \rightarrow CH_4 + 2H_2O$	0.169
$2CO_2 + 8H_2O + 12e^- \rightarrow C_2H_4 + 12OH^-$	0.07
$2CO_2 + 9H_2O + 12e^- \rightarrow C_2H_5OH + 12OH^-$	0.08
$3CO_2 + 13H_2O + 18e^- \rightarrow C_3H_7OH + 18OH^-$	0.09
Other	
$N_2H_4(aq) + 4H_2O + 2e^- \rightarrow 2NH_4^+ + 4OH^-$	0.1
$H_2S(g) + 2h^+ \rightarrow S(s) + 2H^+$	0.144
$SO_2(aq) + 4H^+ + 4e^- \rightarrow S(s) + 2H_2O$	0.50
$H_3AsO_3(aq) + H_2O + 2h^+ \rightarrow H_3AsO_4(aq) + 2H^+$	0.56
$NO_2(g) + H_2O + h^+ \rightarrow NO_3^-(aq) + 2H^+$	0.80
$NO(g) + 2H_2O(l) + 3h^+ \rightarrow NO_3^-(aq) + 4H^+$	0.957
$H_2O_2(aq) + H^+ + e^- \rightarrow H_2O + OH^-$	1.14
$Cr_2O_7^{2-} + 14H^+ + 6e^- \rightarrow 2Cr^{3+} + 7H_2O$	1.36
$HO_2^{\cdot} + H^+ + e^- \rightarrow H_2O_2(aq)$	1.44
$H_2O_2(aq) + 2H^+ + 2e^- \rightarrow 2H_2O$	1.763

a) Superscripts denote standard redox potentials in basic solutions (pH = 14).
Source: Li et al. [176].

reaction (charge utilization) (Figure 1.5). In particular, it is well recognized that the overall photocatalytic quantum efficiency (η_c) is fundamentally determined by the product of efficiencies of the four tandem steps, including light harvesting efficiency (η_{abs}), charge separation efficiency (η_{cs}), charge migration and transport efficiency (η_{cmt}), and charge utilization efficiency (η_{cu}) for H_2 generation. The relationship between them could be calculated according to Eq. (1.2) [127, 151]:

$$\eta_c = \eta_{abs} \times \eta_{cs} \times \eta_{cmt} \times \eta_{cu} \tag{1.2}$$

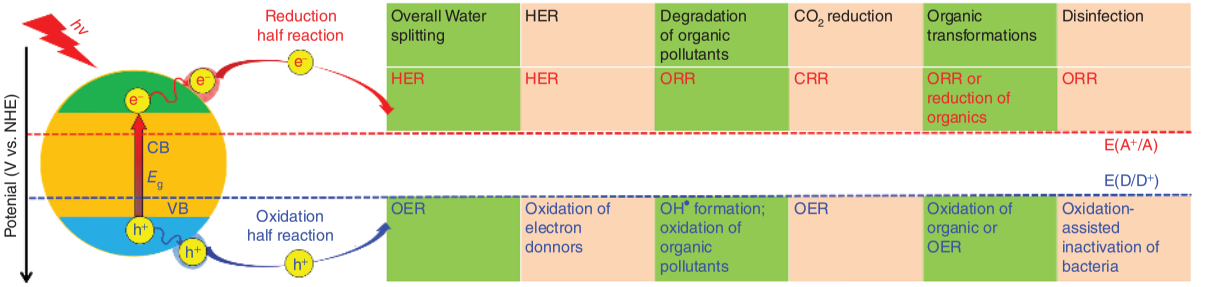

Figure 1.3 The reduction and oxidation half reactions in different photocatalytic reactions. OER, oxygen evolution reaction; HER, hydrogen evolution reaction; ORR, oxygen reduction reaction; and CRR, CO_2 reduction reaction. Source: Li et al. [134].

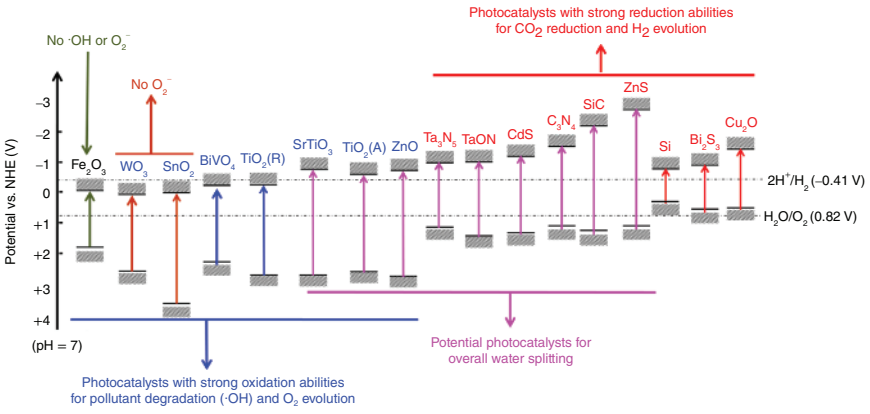

Figure 1.4 Band positions and potential applications of some typical photocatalysts (at pH 7 in aqueous solution). Source: Li et al. [176].

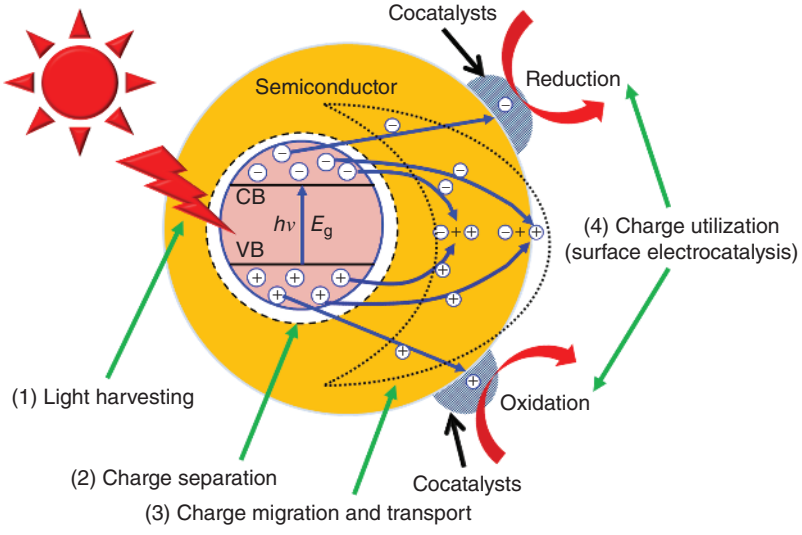

Figure 1.5 Kinetic processes of photocatalysis: (1) light harvesting, (2) the separation of photogenerated electron–hole pairs, (3) the migration and transport of photogenerated electrons and holes, and (4) the surface charge utilization for the reduction and oxidation of adsorbed reactants initiated by highly reactive electrons and holes, respectively. Source: Li et al. [176].

Therefore, to develop highly effective photocatalysts, all kinetic processes in the previously mentioned four steps must be comprehensively considered.

Among these kinetic processes, charge carrier dynamics, including trapping, recombination, and transfer, fundamentally determines their overall photocatalytic efficiency, which is significantly impacted by various factors such as the surface and interface properties, particle size, and shape of semiconductor materials [178]. Accordingly, understanding the charge carrier dynamics in semiconductors plays